



OPEN

SUBJECT AREAS:  
STRUCTURAL MATERIALS  
MECHANICAL PROPERTIES

Received  
11 September 2013

Accepted  
5 February 2014

Published  
28 February 2014

Correspondence and  
requests for materials  
should be addressed to  
Z.H.X. (zonghan.xie@  
adelaide.edu.au)

# Synergistic toughening of hard, nacre-mimetic MoSi<sub>2</sub> coatings by self-assembled hierarchical structure

Jiang Xu<sup>1,2</sup>, Xiaoli Zhao<sup>3</sup>, Paul Munroe<sup>4</sup> & Zonghan Xie<sup>1,5</sup>

<sup>1</sup>School of Mechanical & Electrical Engineering, Wuhan Institute of Technology, Wuhan, 430073, PR China, <sup>2</sup>Department of Material Science and Engineering, Nanjing University of Aeronautics and Astronautics, Nanjing 210016, PR China, <sup>3</sup>School of Engineering, Edith Cowan University, Perth, WA 6027, Australia, <sup>4</sup>School of Materials Science and Engineering, University of New South Wales, Sydney, NSW 2052, Australia, <sup>5</sup>School of Mechanical Engineering, University of Adelaide, Adelaide, SA 5005, Australia.

Like many other intermetallic materials, MoSi<sub>2</sub> coatings are typically hard, but prone to catastrophic failure due to their low toughness at ambient temperature. In this paper, a self-assembled hierarchical structure that closely resembles that of nacre (i.e., mother of pearl) was developed in a MoSi<sub>2</sub>-based coating through a simple, yet cost-effective, deposition technique. The newly formed coating is tough and can withstand multiple indentations at high loads. Key design features responsible for this remarkable outcome were identified. They include a functionally graded multilayer featuring elastic modulus oscillation, varying sublayer thickness and a columnar structure that are able to attenuate stress concentrations; interlocking boundaries between adjacent sublayers that improve the bonding and arrest the cracks; a transitional layer that bridges the coating and substrate and facilitates load transfer. Moreover, the contributions of six important structural characteristics to damage resistance are quantified using finite element analysis and in an additive manner (i.e., from low- to high-level complexity). The *in-situ* toughened coating is envisaged to enhance the mechanical performance and extend the lifespan of metal components used in safety-critical applications.

**A**pplying coatings for surface protection can be traced back more than 20,000 years, when natural materials such as blood, eggs or plant fibres were used<sup>1</sup>. Despite such a long history, major technological advances only took place about half a century ago, when physical vapour deposition was utilized to prepare hard, adherent coatings, significantly enhancing the performance and durability of cutting tools, engine components and biomedical devices<sup>2</sup>.

With the introduction of extremely hard coatings in recent years, catastrophic failure, resulting from their low tolerance to structural defects and damage, has become a limiting factor in safety-critical applications<sup>3,4</sup>. In contrast, a combination of high hardness and good toughness can be found in many naturally occurring materials, for instance, nacre, enamel and bone<sup>5–7</sup>. These materials exhibit a multilayered hierarchical structure, built from mineral crystallites and soft organic compounds<sup>8</sup>. Multiple toughening processes work together to make these biological materials exceptionally resistant to contact damage<sup>9</sup>. In addition, biological interfaces, such as enamel-dentin junctions, exhibit interlocking traits<sup>10</sup>, offering distinct advantages in facilitating load transfer and enhancing interfacial strength<sup>11</sup>.

Over the past several years, considerable efforts have been made to develop hard, yet tough, materials and coatings, often through emulating materials design in nature and backed by theoretical analysis and simulations<sup>12–17</sup>. Multilayered coatings modelled on nacre that comprise alternating hard and soft layers were reported and attracted considerable attention<sup>18–21</sup>. They were commonly fabricated using an additive process, i.e., sequential deposition of hard and soft materials under precisely controlled deposition conditions. The sophisticated procedures required for synthesising these coatings render manufacturing prohibitively expensive for many industrial applications. Additionally, the additive fabrication makes the interfaces potentially weak and vulnerable to fatigue damage. Moreover, unlike their natural counterparts, multiple toughening processes are rarely seen in these synthetic coatings.

Recently, we have developed a bimodally grained microstructure in a MoSi<sub>2</sub>-based coating by using a simple, yet cost-effective, fabrication technique - glow discharge plasma deposition<sup>22</sup>. The resultant coating displays an increased resistance to contact damage through crack bridging and deflection. Driven by this advance, a complex



hierarchical structure was created *in situ* for a MoSi<sub>2</sub>-based composite coating in this study. This newly developed coating captures key design elements of tough biological materials and, as such, possesses a remarkable damage tolerance as well as excellent load-carrying ability. Important structural factors responsible for the improved toughness were modelled and evaluated. The work reported here opens a new pathway to developing hard, yet tough, coatings for safety-critical applications, where catastrophic failure cannot be tolerated.

## Results

Unlike nanocrystalline structures reported for monolithic MoSi<sub>2</sub> and Mo<sub>5</sub>Si<sub>3</sub> coatings<sup>22,23</sup>, in this study a complex multilayer structure was

developed *in-situ* for a MoSi<sub>2</sub>-based composite coating (named here 'MMC'). To reveal its microstructure features, both plan-view and cross-sectional images of the MMC coating were acquired. As shown in Fig. 1a, the coating contains three distinct layers. The outermost layer is ~1 μm thick (refer to the top surface region labelled as "MoSi<sub>2</sub>" in Fig. 1a) and comprises fine MoSi<sub>2</sub> crystals with an average diameter of ~5 nm, according to plan-view TEM shown in Fig. 1b. The fringe spacing of the crystallites, outlined by dotted red circles in Fig. 1b, is 2.18 Å, corresponding to the (111) lattice plane of hexagonal C40-structured MoSi<sub>2</sub>. These fine C40-MoSi<sub>2</sub> grains are arranged with a (111) texture (see XRD data shown in Fig. 1b). Note, the Mo<sub>5</sub>Si<sub>3</sub> peaks in the XRD pattern are supposed to originate from region underneath the outer layer.

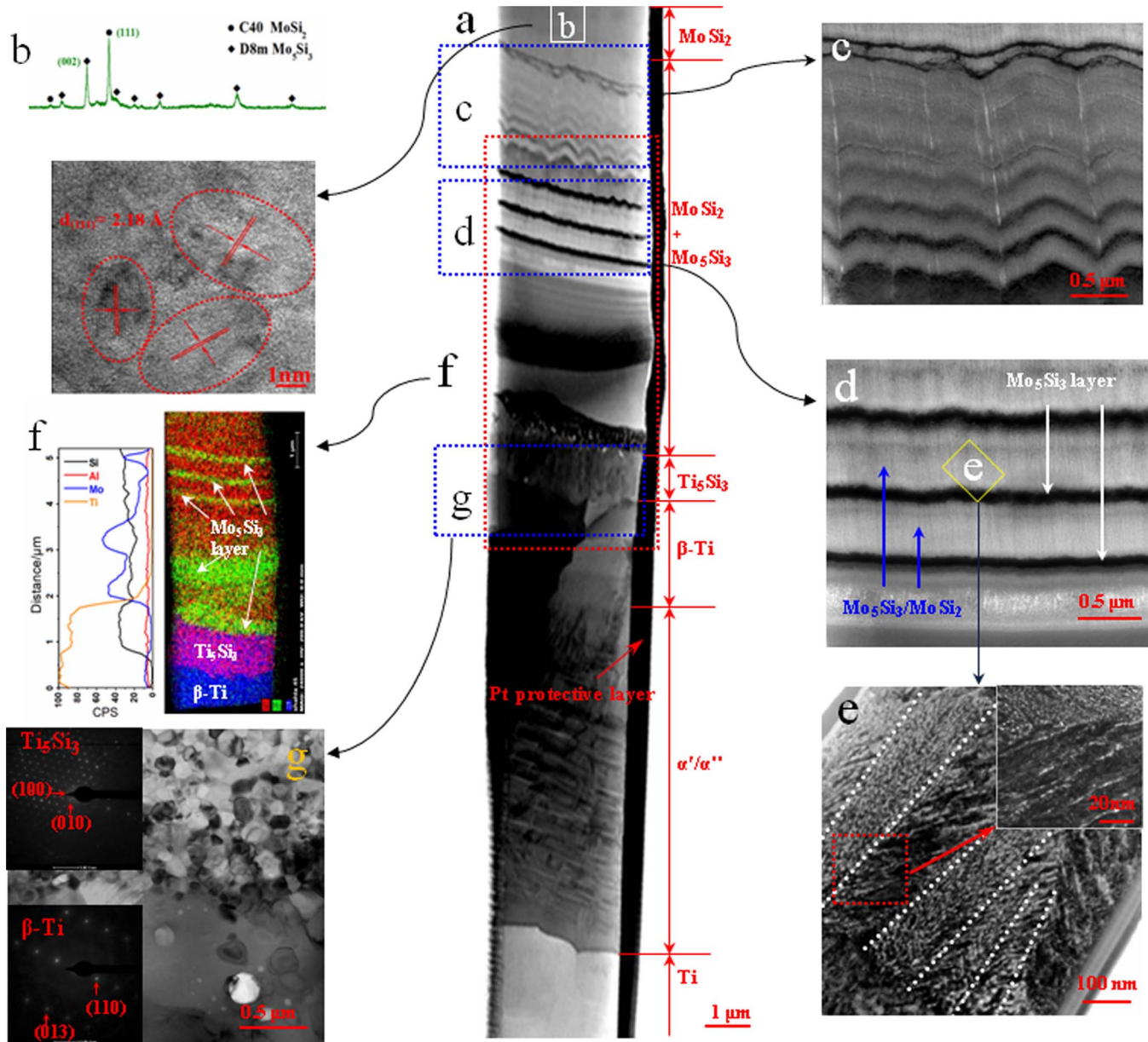


**Figure 1 |** (a) Cross-sectional bright-field transmission electron micrograph (TEM) revealing the pristine microstructure of the MMC coating. (b) X-ray diffraction pattern showing that MoSi<sub>2</sub> is the dominant phase within the outer layer of the coating. Note that the peaks for Mo<sub>5</sub>Si<sub>3</sub> originate presumably from region beneath the outer layer. Below the XRD curve is a plan-view bright-field TEM image taken ~500 nm deep from the surface in region outlined by solid white line in a). (c,d) Enlarged field emission scanning electron microscope (FESEM) images of regions "c" and "d" outlined by dotted blue lines in a). (e) Cross-sectional TEM image of columnar structure of region "e" outlined by solid yellow line in d). (f) 2D elemental mapping of region "f" outlined by dotted red line in a). (g) Cross-sectional TEM image of the junction between the intermediate layer and substrate, as outlined by the dotted blue line "g" in a).

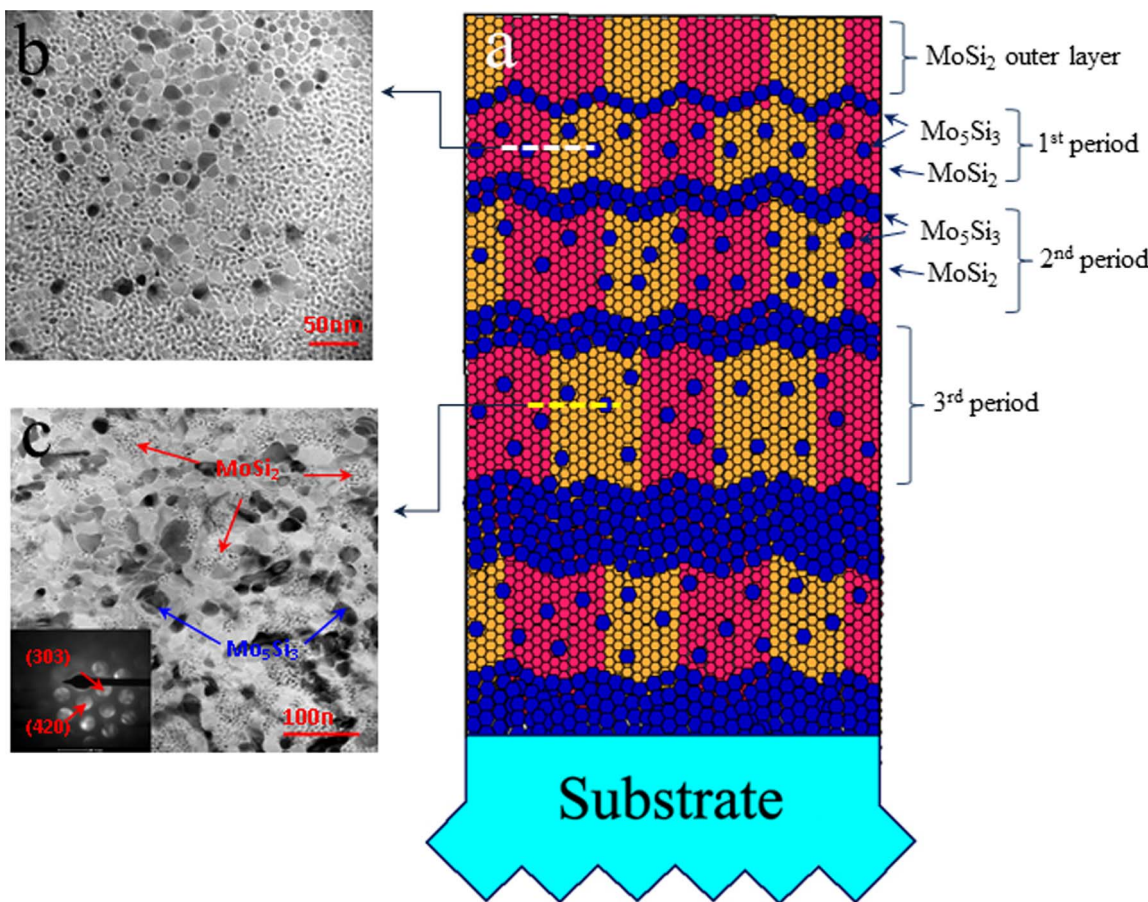


**Figure 2 |** (a) Schematic illustration of the self-assembled multilayer structure in the MMC coating (not drawn to scale). (b) Plan-view bright-field TEM image taken from the area  $\sim 5 \mu\text{m}$  below the surface as indicated by dashed white horizontal line in a). (c) Plan-view bright-field TEM image taken from the area  $\sim 10 \mu\text{m}$  below the surface as indicated by dashed yellow horizontal line in a), with corresponding SAED pattern of “coarser” grains shown in the lower left inset. Note in a), below the outer layer ( $\sim 1 \mu\text{m}$  thick MoSi<sub>2</sub>, refer to Fig. 1a) is the intermediate layer ( $\sim 8.5 \mu\text{m}$  thick, as seen in Fig. 1a) exhibiting a graded, multilayer structure that comprises  $\sim 10$  periods (also refer to Fig. 1a). Each period consists of 2 sublayers; namely, the Mo<sub>5</sub>Si<sub>3</sub> layers (in blue colour, designated as “Sublayers A” in Table 1) and the MoSi<sub>2</sub>-rich columnar layers (in red and yellow, designated as “Sublayers B” in Table 1) with Mo<sub>5</sub>Si<sub>3</sub> grains embedded (in blue).

Below the outer MoSi<sub>2</sub> layer is a  $\sim 8.5 \mu\text{m}$  thick intermediate layer. It exhibits a multilayered structure, in which sublayers interlock with each other. Fig. 1c and 1d are enlarged views of multilayer regions “c” and “d” outlined by dotted blue lines in Fig. 1a. The sublayers lighter in contrast, as further revealed in Fig. 1e, comprise tightly packed, vertically aligned rods, whose boundaries are highlighted by dotted white lines; the individual rods have a diameter of  $\sim 100 \text{ nm}$  and contain highly organized, elongated grains. The plan-view bright-field TEM images of the lighter contrast sublayers, taken from regions about  $5 \mu\text{m}$  and  $10 \mu\text{m}$  below the surface (as indicated in Fig. 2a), are shown in Fig. 2b and 2c, respectively. Both regions exhibit a bimodally grained microstructure: finer grains have a size similar to those in the outer layer and are indeed C40-structured MoSi<sub>2</sub>, whilst coarser grains, according to the associated selected area electron diffraction (SAED) pattern (Fig. 2c, inset), represent the D<sub>8m</sub> Mo<sub>5</sub>Si<sub>3</sub> phase. The size of Mo<sub>5</sub>Si<sub>3</sub> grains increases from  $\sim 50$  to  $\sim 70 \text{ nm}$  with increasing depth, whereas the diameter of MoSi<sub>2</sub> is smaller than  $10 \text{ nm}$  and barely changes throughout the intermediate layer.

To determine the phase composition of the darker contrast sublayers, EDS elemental mapping of region “f” outlined by dotted red line in Fig. 1a is displayed in Fig. 1f. It reveals that these darker contrast sublayers are rich in Mo and Si. Moreover, the ratio of Mo to Si is found to be  $\sim 1.7$ , implying that these sublayers are most likely the Mo<sub>5</sub>Si<sub>3</sub> phase. According to its concentration profile in Fig. 1f,

Mo in the intermediate layer exhibits uphill diffusion behaviour. Uphill diffusion is a common feature of multi-component systems, occurring when the activity gradient of a component is greater and in the opposite direction to its concentration gradient<sup>24</sup>. Uphill diffusion of the Mo element observed here may be explained as a consequence of a negative chemical interaction between Ti and Mo. When the Mo element diffuses toward the coating/substrate interface, the presence of Ti decreases the activity of Mo to the extent that the Mo activity gradient in the intermediate layer is in the opposite direction to the Mo concentration gradient. The phenomenon of uphill diffusion of Mo was also observed in the Me vs. MoSi<sub>2</sub> diffusion couples where Me = W, Re, Nb or Ta<sup>25</sup>. The transitional layer between the intermediate and the substrate is about  $1 \mu\text{m}$  thick (Fig. 1a, region “g”); the main constituent in this region changes from fine Ti<sub>5</sub>Si<sub>3</sub> (the upper half in Fig. 1g) to relatively coarse  $\beta$ -Ti grains (the lower half in Fig. 1g). Below the  $\beta$ -Ti rich layer is a region ( $\sim 7.3 \mu\text{m}$  thick) made of  $\alpha''$  and  $\alpha'$  phases (Fig. 1a). The type of constituents present in this region seems to be closely associated with the Mo contents. The upper part, having a Mo content greater than 6 wt%, is composed of acicular  $\alpha''$  phase, while the lower part is dominated by platelet-like  $\alpha'$  phase.

According to the preceding observation, a sophisticated hierarchical structure that closely resembles that of nacre is developed in the MMC coating, as illustrated in Fig. 2a. The basic building blocks are MoSi<sub>2</sub> and Mo<sub>5</sub>Si<sub>3</sub>. The elongated MoSi<sub>2</sub> grains form rods embedded



with  $\text{Mo}_5\text{Si}_3$ ; each rod is  $\sim 100$  nm in diameter. They are bundled together into layers assuming a columnar structure (as seen in red and yellow colours in Fig. 2a), through which the content of  $\text{Mo}_5\text{Si}_3$  increases. These layers are locked together by  $\text{Mo}_5\text{Si}_3$  sublayers (as seen in blue in Fig. 2a), and thus a functionally graded, multilayer structure results. Unlike those reported in the literature<sup>26,27</sup>, such a nacre-like structure is formed *in situ* in this work. Some striking hallmarks describing the spinodal decomposition of alloys, such as periodic microstructure and compositional fluctuation, are observed in the MMC coating<sup>28</sup>. The spinodal phase segregation during the coating growth is a thermodynamically driven and diffusion-controlled process. To make it occur, high deposition temperature is introduced in this work. However, to understand the spinodal decomposition in the MMC coating, detailed thermodynamical analysis is needed, for example, the determination of the Gibbs free energy of the mixed  $\text{MoSi}_2/\text{Mo}_5\text{Si}_3$  system, which is part of ongoing investigation.

Typical load-displacement curves of instrumented indentation testing on the  $\text{MoSi}_2$ ,  $\text{Mo}_5\text{Si}_3$  and MMC coatings are shown in Fig. 3a. The hardness ( $H$ ) and elastic modulus ( $E$ ) of the coatings, calculated according to the Oliver-Pharr method<sup>29</sup>, are given as a function of the maximum applied load ( $P$ ) in Fig. 3b. The indentation size effect can be seen with lower  $P$  leading to greater  $H$  and  $E$  values. It is probably associated with the strain gradient and/or cracking underneath indenter. The  $H$  values of the MMC coating are greater than those of monolithic  $\text{MoSi}_2$  and  $\text{Mo}_5\text{Si}_3$  coatings. However, the  $E$  values of the MMC coating are comparable to that of  $\text{MoSi}_2$  at lower loads (20 and 50 mN), because the outer layer ( $\sim 1$   $\mu\text{m}$  thick) of the MMC is made of  $\text{MoSi}_2$ . With the increase of indentation load (or depth), the modulus of the MMC is greater than  $\text{MoSi}_2$ . To appreciate how the as-prepared coatings would behave when subjected to indentation loads, five Vickers indentations were performed in a pattern having one surrounded by four others (Fig. 4a-d). The distance between the central indent and any of surrounding ones is about twice the indentation diagonal length. For the monolithic  $\text{MoSi}_2$  and  $\text{Mo}_5\text{Si}_3$  coatings, both edge ring and corner radial cracks are visible at a load of 300 g (Fig. 4a and 4b). In contrast, for the MMC coating, except for ring cracks around the indents, no radial cracks are seen at the indent corners, even at 1000 g (Fig. 4c and 4d). The SEM image in Fig. 4e shows that the annular rings also appear within the indentation site. Such a deformation mode has been observed when indenting hard coatings having a columnar-grained structure<sup>30</sup>, suggesting that the plastic deformation might be enabled by shear sliding in the coating. To obtain a deeper picture of the damage resistance of the MMC coating, the indents created by a Berkovich indenter at 500 mN were sectioned and examined first using an FIB (Fig. 4f) and then by TEM (Fig. 4g). No open cracks can be detected in the subsurface of the MMC coating and the occurrence and arrest of shear sliding is evident  $\sim 3$   $\mu\text{m}$  beneath the indenter. In comparison, subsurface cracks were found to occur and propagate in the  $\text{MoSi}_2$  and  $\text{Mo}_5\text{Si}_3$  coatings with little resistance (Fig. 4h&i). From these observations, the reason that the  $H$  and  $E$  of the MMC coating are greater than the  $\text{MoSi}_2$  is probably due to the formation of cracks in the brittle  $\text{MoSi}_2$  coating (refer to Fig. 4h) that lowers the measurement values. In addition, the  $\text{Mo}_5\text{Si}_3$  layers in the MMC coating serve as physical barriers that enhance the rigidity (i.e., modulus) and hardness of the coating by resisting the sliding of  $\text{MoSi}_2$  grains.

In an earlier paper on TiSiN-based systems by Wo *et al.*<sup>21</sup>, two factors; that is, the shear sliding and modulus oscillation, were utilised in the design of tough coatings. Moving beyond that, numerous structural and mechanical features are identified in this work. To quantify the contributions of key features including the composition/property gradient and the changing thickness of hard sublayers to the remarkable toughness of the MMC coating, finite element analysis was used to evaluate the stress concentration induced by

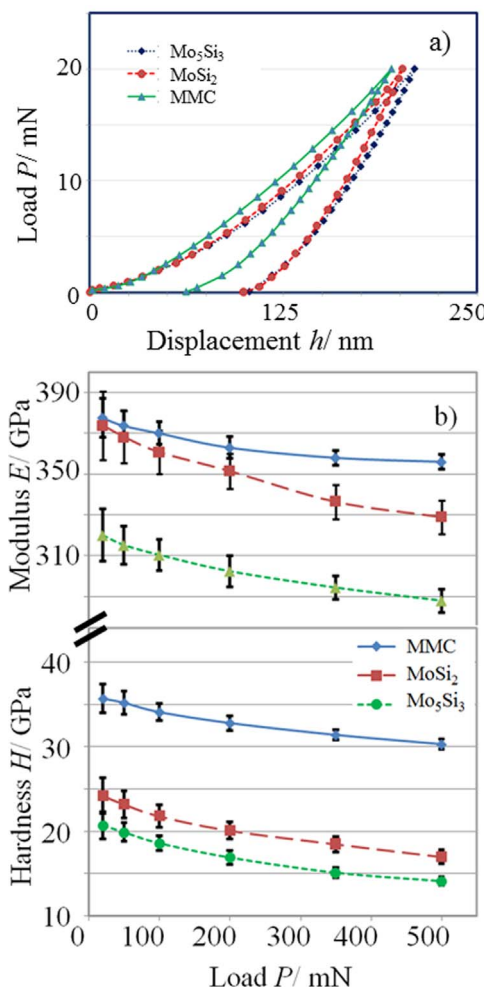


**Figure 3 |** (a) Load-displacement curves of the as-deposited coatings obtained using a Berkovich indenter at a maximum load of 20 mN. (b) The variation of indentation hardness ( $H$ ) and elastic modulus ( $E$ ) of the coatings at different loads. Ten indentations were made at each load, with the results presented here representing average values. Scatter bars representing  $\pm$  one standard deviation are included in the data.

indentation loading in coatings. Seven models with increasing structural complexity, designated as M0 to M6, were constructed: M0 represents a monolithic coating made entirely of  $\text{MoSi}_2$ ; M1 also signifies a monolithic coating made of  $\text{MoSi}_2$  except that a transitional layer is inserted between the coating and substrate; M2 – M6 are multilayer coatings with distinct features in layer thickness, composition and deformation modes (Table 1 and Fig. 2). The mechanical properties of structural components -  $\text{MoSi}_2$  and  $\text{Mo}_5\text{Si}_3$  - used in these models are given in Fig. 3b.

Cracks in hard coatings are normally initiated by either shear or tensile stress. Considering this, the shear stress,  $\tau$ , induced by indentation to a depth of 2.4  $\mu\text{m}$  in the coatings M0-6 are shown Fig. 5. Here the shear stress is defined as  $(\sigma_{11} - \sigma_{33})/2$ , where  $\sigma_{11}$  and  $\sigma_{33}$  are the first and third principal stresses, respectively. In the case of axial symmetry,  $\tau$  is within the  $r$ - $z$  plane, and can be calculated using the equation  $\tau = \{[(\sigma_{rr} - \sigma_{zz})/2]^2 + \tau_{rz}\}^{1/2}$ . Notably, the maximum shear stress appears just below the contact surface, and is concentrated within the  $\text{MoSi}_2$  rich sublayers (due to its higher modulus) in the multilayer coatings (M2-6). A considerable reduction in both the stress magnitude and extent results, when the coating structure changes from monolithic to multilayered. This is particularly true for M6, which bears a striking resemblance to the nacre-like coating prepared in this work. For M6, the material volume populated by

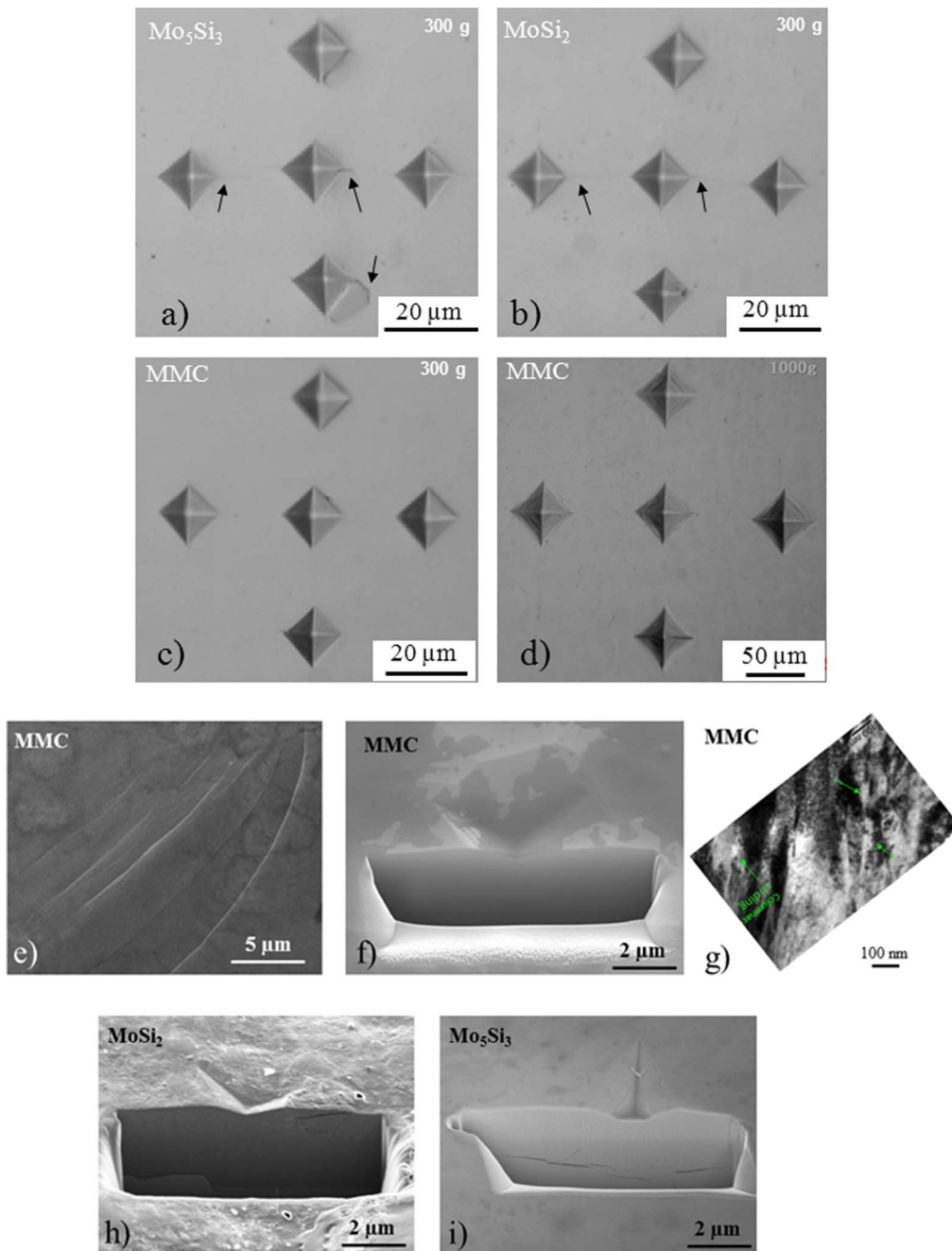


**Figure 4 |** Scanning electron micrograph (SEM) of Vickers indentation patterns created on (a) Mo<sub>5</sub>Si<sub>3</sub> and (b) MoSi<sub>2</sub> at 300 g and on the MMC coating at (c) 300 g and (d) 1000 g. (e) SEM images of the edge of indents in Fig. 4d. Cross-sectional views of the indents created by a Berkovich indenter at 500 mN on (f) MMC, (g) also on MMC, showing the occurrence and arrest of shear sliding in a region ~3 μm deep from the surface, on (h) MoSi<sub>2</sub> and (i) Mo<sub>5</sub>Si<sub>3</sub> coatings.

high shear stress, as shown in red in Fig. 5, is reduced markedly, compared with M0. Such a drop also occurs at other indentation depths modelled in this work. Further, the observed reduction is not only limited to the shear stress. Our modelling results indicate a reduction of all stress components within the multilayered structure (i.e., M6), including the tensile stress and von Mises stress, compared to those in a monolithic coating (i.e., M0).

Fig. 6 provides a quantitative comparison of the material volumes in seven types of coatings that are populated by various shear stress levels. Notably, a consistent reduction in the stress is achieved by gradually increasing the structural complexity (i.e., incorporating new features to the coating design one step at a time). Judging from M0 through to M6, the material volumes populated by shear stress level

equal to or greater than 17.2 GPa are 17.9, 14.6, 14.4, 11.6, 8.8, 4.3 and 1.2 μm<sup>3</sup>, respectively (refer to data in associated Table). In this case, adding a transitional layer (formation of new intermetallic compounds induced by interdiffusion between the coating and substrate) would reduce the stressed volume by ~18% (M1), while subsequent uniform insertion of alternating softer Mo<sub>5</sub>Si<sub>3</sub> layers (i.e., sublayers A in Table 1) with a thickness of 0.2 μm (M2) only brings about a marginal improvement (i.e., ~1.4% over M1). This may be due to a less pronounced modulus oscillation in the multilayer<sup>21,31</sup>. Advancing from M2, M3 features a gradual increase in the thickness of the Mo<sub>2</sub>Si layers (i.e., the sublayers B in Table 1), which results in a reduction of stressed volume by ~35% over M0. Comparing with M3, the elastic modulus for the sublayers B is lowered in M4 from



**Table 1 | Physical parameters used in the FEA and explanation of increased structural complexity from M0 to M6. Refer to Figure 2 for illustration of the multilayer structure**

Model	Sublayers A		Sublayers B		Structural feature added <sup>e)</sup>
	Thickness (μm)	Material	Thickness (μm)	Material	
M0 <sup>a)</sup>	-	-	-	-	Monolayer
M1 <sup>b)</sup>	-	-	-	-	Transition layer
M2	0.2	Mo <sub>5</sub> Si <sub>3</sub>	0.65	MoSi <sub>2</sub>	B-layers: thickness constant
M3	0.2	Mo <sub>5</sub> Si <sub>3</sub>	0.2+(n-1) × 0.1 <sup>c)</sup>	MoSi <sub>2</sub>	B-layers: thickness varied
M4	0.2	Mo <sub>5</sub> Si <sub>3</sub>	0.2+(n-1) × 0.1	50% MoSi <sub>2</sub> + 50% Mo <sub>5</sub> Si <sub>3</sub>	B-layers: E reduced & constant
M5	0.2	Mo <sub>5</sub> Si <sub>3</sub>	0.2+(n-1) × 0.1	x% MoSi <sub>2</sub> + y% Mo <sub>5</sub> Si <sub>3</sub> <sup>d)</sup>	B-layers: E gradually reduced
M6	0.2	Mo <sub>5</sub> Si <sub>3</sub>	0.2+(n-1) × 0.1	x% MoSi <sub>2</sub> + y% Mo <sub>5</sub> Si <sub>3</sub> <sup>d)</sup>	B-layers: sliding enabled

<sup>a)</sup>Monolayer coating made entirely of MoSi<sub>2</sub> having a thickness of 10.5 μm.  
<sup>b)</sup>Coating comprising a 9.5 μm thick MoSi<sub>2</sub> outer layer, plus a 1 μm thick transitional layer that bridges the coating and substrate. The transitional layer also exists in M2-M6 and its elastic modulus (E) changes linearly from the top [E<sub>MoSi2</sub>] to the bottom [E<sub>steel</sub>].  
<sup>c)</sup>n is the sequential number of the layer, counting from the top (1) to the bottom (10).  
<sup>d)</sup>From the top to bottom sublayers, x = 95, 85, 75, 65, 55, 45, 35, 25, 15 and 5%, respectively. x + y = 100%.  
<sup>e)</sup>The increase of structural complexity from one level to another is explained.

$E_{MoSi2}$  to  $(E_{MoSi2} + E_{Mo5Si3})/2$  by varying composition, yielding a reduction in affected volume by ~51% over M0. For M5, the material volume associated with a stress 17.2 GPa or higher is reduced by ~76% over M0, which demonstrates that a gradual change in the elastic modulus of the sublayers B across thickness (i.e., from  $E_{MoSi2}$  to  $E_{Mo5Si3}$ ) is more effective than simply fixing the modulus of the sublayers B to the average value (as seen in M4). Finally, in the case of M6, in which the inelastic deformation occurs through shear sliding of the columnar elements in sublayers B, the extent of stress concentration is reduced markedly by ~93% to only one-fifteenth that in M0. Furthermore, finite element calculation was conducted to quantify the load-carrying performance of the MMC coating. The results show that for the stress in the MMC to reach the same level as that in the monolithic coating (i.e., M0), about a 70% increase in applied load is required. This means that the MMC coating not only provides remarkable damage resistance, but also possesses excellent load-carrying ability.

The current trend in the development of nacre-mimetic materials and coatings is to mimic ‘mortar-and-brick’ structure of nacre. The resultant microstructure typically consists of hard ceramic platelets bonded together by polymer<sup>18,19,32,33</sup>. While such a design can enhance toughness, it is not suitable for applications involving extreme conditions, such as high speed machining where temperature may rise quickly under heavy load. To combat this challenge, the polymer component can be replaced by stronger, heat-resistant metals or ceramics<sup>15–17</sup>. In view of this, the MoSi<sub>2</sub>-based coatings

comprising alternating layers of hard, thicker MoSi<sub>2</sub> and relatively soft Mo<sub>5</sub>Si<sub>3</sub> layers are developed in the present work. While the effect of elastic modulus oscillation may be less pronounced in this multi-layer structure, additional design features are introduced to ensure remarkable damage resistance can be achieved.

Key toughening mechanisms enabled by the self-assembled hierarchical structure in the MMC coating can be described as follows: under initial contact, the functionally graded structure, created primarily by a continuous increase in Mo<sub>5</sub>Si<sub>3</sub> volume through the coating thickness, promotes the load transfer and, in so doing, discourage the stress build-up in the coating and at the coating/substrate interface. With an increase in load, deformation takes place through the plastic deformation of Mo<sub>5</sub>Si<sub>3</sub> components and/or the shear sliding in the columnar sublayers. The sliding process, once activated, can effectively mitigate the stress concentration without compromising the structural integrity of coating. For TiSiN-based coatings studied by Wo *et al.*<sup>21</sup>, the columnar layers consist of vertically aligned TiN grains. In comparison, in the newly formed coating the columnar layers exhibit a hierarchical structure that comprises tightly packed rods; each has a diameter of ~100 nm and contains highly organized, elongated MoSi<sub>2</sub> grains. Consequently, shear deformation could occur at both ‘rod’ and ‘grain’ levels under high loads, making the new coating even tougher. It is also worth noting that Mo<sub>5</sub>Si<sub>3</sub> sublayers have two functions: a) they serve as a physical barrier that resists the shear deformation of columnar sublayers, simultaneously increasing the stiffness, hardness and damage tolerance of coating; b)

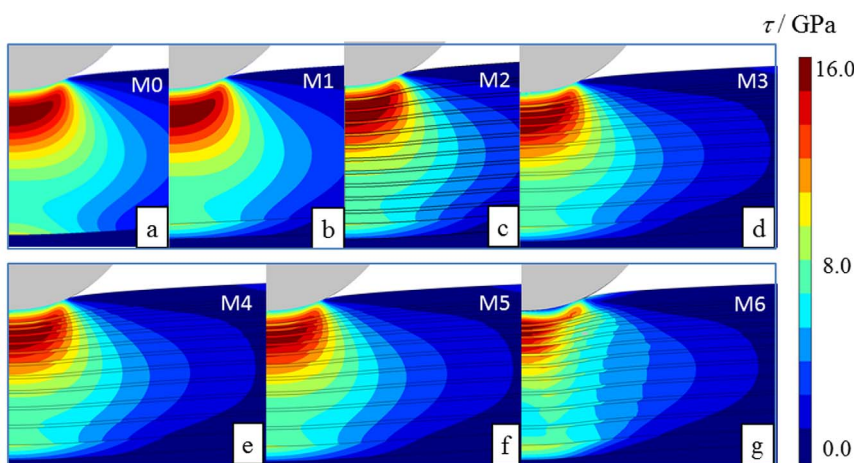
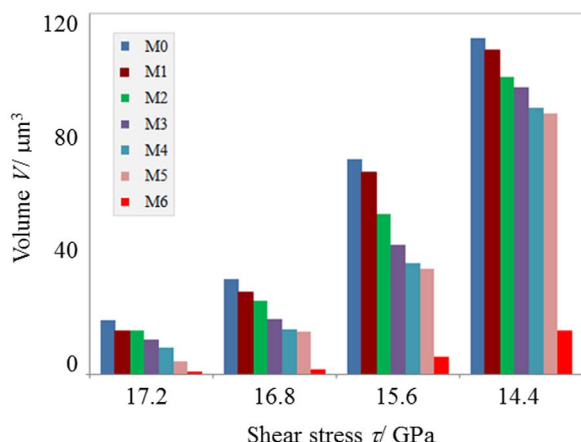


**Figure 5 |** The distribution of the shear stress,  $\tau$ , obtained by FEA in (a) M0, (b) M1, (c) M2, (d) M3, (e) M4, (f) M5 and (g) M6 at an indentation depth of 2.4 μm.



**Material volume populated by stress levels equal to or greater than 17.2 GPa**

Coating model	M0	M1	M2	M3	M4	M5	M6
Structural feature added	Monolayer	Transition layer	B-layers: thickness constant	B-layers: thickness varied	B-layers: E reduced & constant	B layers: E gradually reduced	B layers: sliding enabled
Material volume, $\mu\text{m}^3$	17.9	14.6	14.4	11.6	8.8	4.3	1.2
% reduction in vol. over M0	/	18.4%	19.6%	35.2%	50.8%	76.0%	93.3%

**Figure 6 |** Material volume populated by different levels of shear stress in various coating structures (M0–M6) at an indentation depth of 2.4  $\mu\text{m}$ . Data displayed in Table are an example showing material volume populated by stress stresses equal to or greater than 17.2 GPa.

they interlock with columnar sublayers, giving rise to extended interfacial area with strong chemical bonds, and are particularly effective in arresting lateral cracks.

The relative thickness of soft and hard materials in a multilayer structure has an appreciable effect on its damage resistance. Theoretical analysis<sup>34</sup> and subsequent experimental observation<sup>35</sup> have shown that hard, thicker layers alternated by thin, softer layers is most effective in resisting the crack propagation. Distinctly different from TiSiN-based systems studied earlier by Wo *et al.*<sup>21</sup> that features a less favourable design, i.e., soft thicker layers (TiN) separated by thin harder ones (TiSiN), here the new MoSi<sub>2</sub>-based composite coating exhibits a preferred modulus oscillation profile - hard, thicker layers (MoSi<sub>2</sub> dominated) separated by thin, softer layers (Mo<sub>5</sub>Si<sub>3</sub>). Moreover, with an increase in depth, the thickness of hard MoSi<sub>2</sub> dominated sublayers increases, further enhancing the crack resistance. Last, but not least, a transitional layer is developed between the coating and substrate from the inter-diffusion of Mo and Ti elements. Its presence not only provides strong bonding that unites the coating with the substrate, but also further lowers the stress concentration at the coating/substrate interface.

## Discussion

In summary, a MoSi<sub>2</sub>-based coating having a layered, nacre-like structure was synthesized *in situ* by using a simple, yet economic, fabrication technique - glow discharge plasma deposition. Indentation experiments show that the newly-developed coating possesses a remarkable resistance to contact damage. Finite element analysis demonstrates that effective lines of defence against damage exist in the coating, stemming from its self-toughened architecture. That is, a) a functionally graded multilayer, with elastic modulus oscillation that lowers the stress concentration that otherwise drives crack growth in the coating; b) the columnar substructure that enables inelastic deformation through shear sliding that dissipates energy;

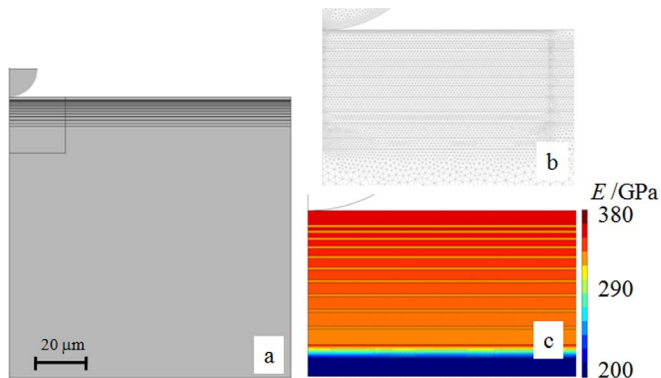


**Figure 7 | Model configuration used in FEA.** (a) The geometry of the model, (b) details of locally refined mesh elements in the coatings, and (c) the modulus distribution in the MMC coating.

c) relatively soft Mo<sub>5</sub>Si<sub>3</sub> layers that enhance the bonding through interlocking and act as physical barriers against the shearing of columnar layers; d) the transitional layer that welds the coating and substrate together and promotes the load transfer through the coating/substrate interface. This work represents a notable technological advance in the synthesis and characterisation of bio-inspired, damage-resistant coatings that have potential to enhance the performance and durability of metal components operating under severe loading conditions.

## Methods

Substrate discs, 40 mm in diameter and 3 mm in thickness, were cut from a commercially pure titanium rod (0.003% N, 0.010% C, and 0.074% O). Prior to coating deposition, the substrates were ground successively using SiC grinding papers of 400, 800, 1200 grades and, finally, polished with 1.5  $\mu\text{m}$  diamond paste. The polished substrates were then ultrasonically cleaned in ethyl alcohol and dried in cold air. The MoSi<sub>2</sub>-based composite coating (termed here MMC) was deposited onto the substrate using a double cathode glow discharge apparatus, wherein a target having a stoichiometric ratio of Mo<sub>30</sub>Si<sub>70</sub> was mounted. For comparison, monolithic MoSi<sub>2</sub> and Mo<sub>5</sub>Si<sub>3</sub> coatings were also deposited from targets having stoichiometric ratios of Mo<sub>25</sub>Si<sub>75</sub> and Mo<sub>50</sub>Si<sub>50</sub>, respectively. The targets were fabricated from ball-milled Mo (99.99% purity) and Si powders (99.99% purity) by cold compaction under a pressure of 600 MPa. During deposition, one cathode was the target, and the other was the substrate<sup>36</sup>. The glow discharge sputtering conditions can be described as follows: the base pressure,  $4 \times 10^{-4}$  Pa; target electrode bias voltage, -950 V; substrate electrode bias voltage, -400 V; working pressure, 35 Pa; target-substrate distance, 10 mm; and treatment time 3 h. The substrate temperature was set at  $\sim 800^\circ\text{C}$  for the deposition of monolithic MoSi<sub>2</sub> and Mo<sub>5</sub>Si<sub>3</sub> coatings and at  $\sim 900^\circ\text{C}$  for the MMC coating.

The phase composition of the as-grown coatings was characterized with an X-ray diffractometer (XRD, D8 Advance, BRUKER AXS, Inc., Madison, WI 53711-5373, USA) operating at 35 kV and 40 mA. X-ray data were collected using a 0.1° step scan with a count time of 1 s. To reveal the microstructural features of coatings, plan-view samples for transmission electron microscope (TEM) observation were prepared using a single-jet polishing technique from the untreated side of the substrate<sup>22</sup>. The cross-sectional TEM samples were also prepared using a focused ion beam (FIB) microscope (FEI 200xP, FEI instrument, Hillsboro, USA) by sectioning through the area of interest. Detailed descriptions of the procedure can be found elsewhere<sup>37,38</sup>. These samples were examined using a field emission gun TEM (Philips CM200, Eindhoven, Netherlands) operating at 200 kV. An energy dispersive X-ray spectrometer (EDS) was interfaced to the TEM for elemental analysis. The crystal structure of the coatings was determined from selected-area electron diffraction (SAED) analysis. To investigate the damage patterns in the coatings, the surface and subsurface examination of indentations was performed using the FIB microscope and TEM.

Instrumented indentation tests were conducted on the as-prepared coatings using a Berkovich indenter (NHT, CSEM Instruments, Switzerland). Fused silica was used as standard material in calibration. The load-displacement curves were obtained by driving the indenter with a constant loading rate of 40 mN/min into the samples at maximum loads ranging from 20 to 500 mN. The hardness and the elastic modulus of the coatings were calculated using the Oliver-Pharr method<sup>29</sup>. The damage tolerance of the as-deposited coatings was evaluated by a Vickers indenter over a range of loads up to 1000 g.

Finite element analysis (FEA) was performed using COMSOL software to elucidate the roles of key microstructural features in mitigating the stress level and maintaining the structural integrity of the coatings. To do that a two-dimensional axisymmetric model of  $100 \times 100 \mu\text{m}$  was constructed (Fig. 7a). It consists of a coating and substrate assembly that was loaded along the z axis by a diamond spherical indenter



with a radius of 10  $\mu\text{m}$ . The thickness of the coatings is 10.5  $\mu\text{m}$ . For coatings having a layered structure that mimics the MMC coating, they consist of an outer layer of 1  $\mu\text{m}$  in thickness and an intermediate layer having 10 ‘periods’. According to Table 1 and Fig. 2, each period consists of two sublayers – A and B. The sublayer A in each period maintains a constant thickness, i.e., 0.2  $\mu\text{m}$ , while the thickness of sublayer B increases by an interval 0.1  $\mu\text{m}$  from the 1st (0.2  $\mu\text{m}$  thick) to the 10th period (1.1  $\mu\text{m}$  thick). To account for interdiffusion induced formation of new intermetallic compounds between the coating and substrate, a transitional layer (1  $\mu\text{m}$  thick) having a gradient modulus is also introduced in the FEA simulations.

To ensure high accuracy around the stress concentration zone, a refined mesh was used within an area of  $20 \times 20 \mu\text{m}$  of the coating directly underneath the indenter (Fig. 7b). The total number of mesh elements is 40730, which includes the elements within the indenter. Further mesh refinement did not improve the simulation results significantly. Time-dependent deformation, such as creep, was not considered in the simulations. The contact between the indenter and the sample was assumed to be frictionless. Boundary conditions can be described as follows<sup>31,39</sup>: the bottom of the simulation block is fixed in the z direction, while the right edge of the block is fixed in the x direction. The left edge of the block coincides with the axisymmetric axis in order to generate 3D results. The indenter tip was positioned at  $z = 0 \mu\text{m}$  before indentation. The indentation process was simulated as the downward displacement of the indenter tip from  $0 \sim 2.4 \mu\text{m}$  at a step of 0.2  $\mu\text{m}$ .

The sublayers A (made of  $\text{Mo}_5\text{Si}_3$ ) in the multilayer coatings are treated as an isotropic elastic material in simulations. In comparison, the sublayers B (dominated by elongated  $\text{MoSi}_2$  grains) exhibit a columnar microstructure, and shear sliding would occur if the threshold stress is reached under indentation loading. Consequently, the sublayers B are treated as an anisotropic elastic–plastic material in simulations. The threshold stress governing the sliding in the sublayers B can be derived experimentally from the relationship of indentation hardness vs load for the MMC coating (Fig. 3b)<sup>21</sup>. It was estimated to be  $\sim 9.1 \text{ GPa}$ . Fig. 7c shows the modulus distribution over the thickness of the MMC coating.

- Matheson, R. R. 20th-to 21st-century technological challenges in soft coatings. *Science* **297**, 976–979 (2002).
- Bunshah, R. F. *Handbook of Hard Coatings: Deposition Technologies, Properties and Applications* (William Andrew Publishing, New York, 2002).
- Ritchie, R. O. The conflicts between strength and toughness. *Nat. Mater.* **10**, 817–822 (2011).
- Zhang, S. *et al.* Hard yet Tough Nanocomposite Coatings—Present Status and Future Trends. *Plasma Processes Polym.* **4**, 219–228 (2007).
- Kamat, S., Su, X., Ballarini, R. & Heuer, A. Structural basis for the fracture toughness of the shell of the conch *Strombus gigas*. *Nature* **405**, 1036–1040 (2000).
- Gupta, H. S. *et al.* Cooperative deformation of mineral and collagen in bone at the nanoscale. *Proc. Nat. Acad. Sci.* **103**, 17741–17746 (2006).
- Xie, Z., Swain, M. V. & Hoffman, M. J. Structural integrity of enamel: experimental and modeling. *J. Dent. Res.* **88**, 529–533 (2009).
- Fratzl, P. & Weinkamer, R. Nature’s hierarchical materials. *Prog. Mater Sci.* **52**, 1263–1334 (2007).
- Xu, Z. H. & Li, X. Deformation strengthening of biopolymer in nacre. *Adv. Funct. Mater.* **21**, 3883–3888 (2011).
- He, L.-H. & Swain, M. V. Enamel—A functionally graded natural coating. *Journal of dentistry* **37**, 596–603 (2009).
- Zhang, Y. *et al.* Bio-inspired interfacial strengthening strategy through geometrically interlocking designs. *J. Mech. Behav. Biomed. Mater.* **15**, 70–77 (2012).
- Xie, Z. *et al.* Deformation mechanisms of TiN multilayer coatings alternated by ductile or stiff interlayers. *Acta Mater.* **56**, 852–861 (2008).
- Singh, R. K. *et al.* Design of functionally graded carbon coatings against contact damage. *Thin Solid Films* **518**, 5769–5776 (2010).
- Gao, H. *et al.* Materials become insensitive to flaws at nanoscale: lessons from nature. *Proc. Nat. Acad. Sci.* **100**, 5597–5600 (2003).
- Ji, B., Gao, H. & Wang, T. Flow stress of biomorphous metal–matrix composites. *Mater. Sci. Eng., A* **386**, 435–441 (2004).
- Kauffmann, F. *et al.* A quantitative study of the hardness of a superhard nanocrystalline titanium nitride/silicon nitride coating. *Scr. Mater.* **52**, 1269–1274 (2005).
- Broedling, N. C., Hartmaier, A., Buehler, M. J. & Gao, H. The strength limit in a bio-inspired metallic nanocomposite. *Journal of the Mechanics and Physics of Solids* **56**, 1086–1104 (2008).
- Podsiadlo, P. *et al.* Ultrastrong and stiff layered polymer nanocomposites. *Science* **318**, 80–83 (2007).
- Bonderer, L. J., Studart, A. R. & Gauckler, L. J. Bioinspired design and assembly of platelet reinforced polymer films. *Science* **319**, 1069–1073 (2008).
- Schlögl, M. *et al.* Effects of structure and interfaces on fracture toughness of CrN/AlN multilayer coatings. *Scr. Mater.* **68**, 917–920 (2013).

- Wo, P. C. *et al.* Extremely hard, damage-tolerant ceramic coatings with functionally graded, periodically varying architecture. *Acta Mater.* **61**, 193–204 (2013).
- Xu, J., Mao, X., Xie, Z.-H. & Munroe, P. Damage-tolerant, hard nanocomposite coatings enabled by a hierarchical structure. *J. Phys. Chem. C* **115**, 18977–18982 (2011).
- Xu, J. *et al.* Effect of Al addition upon mechanical robustness and corrosion resistance of  $\text{Mo}_5\text{Si}_3/\text{MoSi}_2$  gradient nanocomposite coatings. *Surf. Coat. Technol.* **223**, 115–125 (2013).
- van der Laan, S., Zhang, Y., Kennedy, A. K. & Wyllie, P. J. Comparison of element and isotope diffusion of K and Ca in multicomponent silicate melts. *Earth and planetary science letters* **123**, 155–166 (1994).
- Tortorici, P. & Dayananda, M. Interdiffusion and diffusion structure development in selected refractory metal silicides. *Mater. Sci. Eng., A* **261**, 64–77 (1999).
- Rizzo, A. *et al.* RF sputtering deposition of alternate TiN/ZrN multilayer hard coatings. *Thin Solid Films* **515**, 500–504 (2006).
- Warcholinski, B., Gilewicz, A., Kuklinski, Z. & Myslinski, P. Hard CrCN/CrN multilayer coatings for tribological applications. *Surf. Coat. Technol.* **204**, 2289–2293 (2010).
- Michaelsen, C. On the structure and homogeneity of solid solutions: the limits of conventional x-ray diffraction. *Philosophical Magazine A* **72**, 813–828 (1995).
- Oliver, W. C. & Pharr, G. M. Improved technique for determining hardness and elastic modulus using load and displacement sensing indentation experiments. *J. Mater. Res.* **7**, 1564–1583 (1992).
- Xie, Z., Hoffman, M., Moon, R. & Munroe, P. Deformation of a hard coating on ductile substrate system during nanoindentation: Role of the coating microstructure. *J. Mater. Res.* **21**, 437–447 (2006).
- Zhao, X., Xie, Z. & Munroe, P. Nanoindentation of hard multilayer coatings: Finite element modelling. *Mater. Sci. Eng., A* **528**, 1111–1116 (2011).
- Munch, E. *et al.* Tough, bio-inspired hybrid materials. *Science* **322**, 1516–1520 (2008).
- Tushtev, K. *et al.* A Novel Bioinspired Multilayered Polymer–Ceramic Composite with Outstanding Crack Resistance. *Advanced Engineering Materials*, DOI: 10.1002/adem.201300204 (2013).
- Fratzl, P., Gupta, H. S., Fischer, F. D. & Kolednik, O. Hindered crack propagation in materials with periodically varying Young’s modulus—lessons from biological materials. *Advanced Materials* **19**, 2657–2661 (2007).
- Weaver, J. C. *et al.* The stomatopod dactyl club: a formidable damage-tolerant biological hammer. *Science* **336**, 1275–1280 (2012).
- Xu, J., Wang, Y. & Jiang, S. The effects of substitution of Cr for Mo on the mechanical properties of nanocrystalline  $\text{Mo}_5\text{Si}_3$  films. *Nanoscale* **2**, 394–398 (2010).
- Wo, P. C. *et al.* A novel technique for microstructure characterization of garnet films. *Opt. Mater.* **32**, 315–322 (2009).
- Xie, Z.-H., Munroe, P., Moon, R. & Hoffman, M. Characterization of surface contact-induced fracture in ceramics using a focused ion beam miller. *Wear* **255**, 651–656 (2003).
- Li, Z. *et al.* Designing superhard, self-toughening CrAlN coatings through grain boundary engineering. *Acta Mater.* **60**, 5735–5744 (2012).

## Acknowledgments

J.X. acknowledges the financial support of the National Natural Science Foundation of China under Grant No. 51175245 and No. 51374130 and the Aeronautics Science Foundation of China under Grant No. 2013ZE52058.

## Author contributions

J.X. and P.M. carried out all the experiments. J.X. drafted the experiment and some of results part and prepared Fig. 1–4. X.Z. performed the FEA modelling, drafted the FEA section and prepared Fig 5–7. Z.X. coordinated the study and wrote the main manuscript text. All authors reviewed the manuscript.

## Additional information

**Competing financial interests:** The authors declare no competing financial interests.

**How to cite this article:** Xu, J., Zhao, X.L., Munroe, P. & Xie, Z.H. Synergistic toughening of hard, nacre-mimetic  $\text{MoSi}_2$  coatings by self-assembled hierarchical structure. *Sci. Rep.* **4**, 4239; DOI:10.1038/srep04239 (2014).

This work is licensed under a Creative Commons Attribution-NonCommercial-ShareAlike 3.0 Unported license. To view a copy of this license, visit <http://creativecommons.org/licenses/by-nc-sa/3.0>